AGU PUBLICATIONS

JGR

Journal of Geophysical Research: Solid Earth

RESEARCH ARTICLE
10.1002/2015JB012205

Key Points:
- A data-constrained, frequency-dependent, log-quadratic *Pn* spreading model
- Apparent *Pn* wave attenuation in Northeast China and the Korean Peninsula
- Uppermost mantle *P* wave attenuation model in the region

Correspondence to:
L.-F. Zhao,
zhaolf@mail.iggcas.ac.cn

Citation:
Zhao, L.-F., X.-B. Xie, B.-F. Tian, Q.-F. Chen, T.-Y. Hao, and Z.-X. Yao (2015), *Pn* wave geometrical spreading and attenuation in Northeast China and the Korean Peninsula constrained by observations from North Korean nuclear explosions, *J. Geophys. Res. Solid Earth*, *120*, 7558–7571, doi:10.1002/2015JB012205.

Received 12 MAY 2015
Accepted 6 OCT 2015
Accepted article online 10 OCT 2015
Published online 6 NOV 2015

Pn wave geometrical spreading and attenuation in Northeast China and the Korean Peninsula constrained by observations from North Korean nuclear explosions

Lian-Feng Zhao[1], Xiao-Bi Xie[2], Bao-Feng Tian[3], Qi-Fu Chen[1], Tian-Yao Hao[1], and Zhen-Xing Yao[1]

[1]Key Laboratory of Earth and Planetary Physics, Institute of Geology and Geophysics, Chinese Academy of Sciences, Beijing, China, [2]Institute of Geophysics and Planetary Physics, University of California, Santa Cruz, California, USA, [3]Institute of Geophysics, China Earthquake Administration, Beijing, China

Abstract We investigate the geometric spreading and attenuation of seismic *Pn* waves in Northeast China and the Korean Peninsula. A high-quality broadband *Pn* wave data set generated by North Korean nuclear tests is used to constrain the parameters of a frequency-dependent log-quadratic geometric spreading function and a power law *Pn Q* model. The geometric spreading function and apparent *Pn* wave *Q* are obtained for Northeast China and the Korean Peninsula between 2.0 and 10.0 Hz. Using the two-station amplitude ratios of the *Pn* spectra and correcting them with the known spreading function, we remove the contributions of the source and crust from the apparent *Pn Q* and retrieve the *P* wave attenuation information along the pure upper mantle path. We then use both *Pn* amplitudes and amplitude ratios in a tomographic approach to obtain the upper mantle *P* wave attenuation in the studied area. The *Pn* wave spectra observed in China are compared with those recorded in Japan, and the result reveals that the high-frequency *Pn* signal across the oceanic path attenuated faster compared with those through the continental path.

1. Introduction

The seismic *Pn* wave typically appears as the first arrival in regional seismograms at distances between 200 and 2000 km. Unlike other regional phases, such as *Pg* and *Lg* waves, the *Pn* wave is typically less affected by the crustal structures or contaminated by prior phases and is therefore widely applied for seismic location, magnitude, and yield estimation and for investigating seismic source process. The *Pn* wave attenuation measurement is an important issue as well not only because obtaining accurate source parameters requires correction for the amplitude decay but also because attenuation itself can be useful for characterizing the upper mantle properties. *Pn* and *Sn* waves cannot be simply explained as head waves developed along a flat Moho discontinuity. Their actual propagation processes, particularly their amplitude variations in a spherical Earth, are much more complicated. *Červený and Ravindra* [1971] and *Hill* [1973] theoretically investigated the behavior of *Pn* waves in a spherical Earth model and regarded this phase as an interference of multiple-diving waves refracted from the underside of the Moho discontinuity. *Sereno and Given* [1990] studied *Pn* waves in flat and spherical Earth models and found that Earth's sphericity alone causes a significant departure in *Pn* geometrical spreading and that the phenomenon is frequency dependent. Based on numerical simulations, *Yang et al.* [2007] proposed a log-quadratic model for *Pn* and *Sn* geometric spreading functions to accommodate the Earth's sphericity. Compared with the traditional power law model, their spreading model included nine parameters to address both distance and frequency dependencies.

Many attempts have been targeted at using observed data to constrain *Pn* wave attenuation and geometrical spreading [*Chun et al.*, 1989; *Sereno et al.*, 1988; *Xie*, 2007; *Xie and Patton*, 1999; *Zhu et al.*, 1991]. The underlying difficulties are that attenuation and geometrical spreading are tightly coupled and both are dependent on distance and frequency. In addition, the observed *Pn* amplitudes are highly scattered due to their narrow sampling of radiation patterns, inaccurate source locations, and pronounced sensitivity to the uppermost mantle structures. Different strategies were adopted to mitigate this difficulty. By assuming a frequency-independent spreading function of $\Delta^{-1.3}$, where Δ is the distance, *Sereno et al.* [1988] investigated the *Pn* wave *Q* in Scandinavia and obtained a Q_0 (1 Hz *Q*) of 325. Using the same spreading function, *Xie and Patton* [1999] obtained a Q_0 of 364 for central Asia, and *Xie* [2007] observed low *Pn Q* under the north central Tibetan plateau between 0.3 and 10.0 Hz. *Chun et al.* [1989] determined the high-frequency *Pn* attenuation in

Table 1. Event Parameters Used in This Study

North Korean Nuclear Test	Date (yyyy/mm/dd)	Time (UTC)	Latitude (°N)	Longitude (°E)	Depth (km)	m_b (USGS)
NKT1	2006/10/09	01:35:28.00	41.287	129.108	0.0	4.2
NKT2	2009/05/25	00:54:43.11	41.294	129.077	0.0	4.7
NKT3	2013/02/13	02:57:51.27	41.292	129.073	0.0	5.1

eastern Canada based on a frequency-dependent *Pn* spreading $\Delta^{-(2.2+0.02\cdot f)}$ between 3.0 and 15.0 Hz. *Zhu et al.* [1991] simultaneously estimated both frequency-dependent geometric spreading and *Q* for *Pn* waves in the Canadian shield.

Others attempted to estimate the *Pn* or *Sn* wave propagation efficiency without apparently addressing the geometric spreading. *Calvert et al.* [2000] measured the propagation efficiency by separating the attenuation into the average portion and the perturbation portion, avoiding defining the absolute attenuation measurement. Using the ratio of the *Sn* amplitude to the *Pg* coda amplitude, *Barron and Priestley* [2009] presented the frequency-dependent propagation efficiency of the *Sn* wave over the Tibetan Plateau. By stacking the densely distributed USArray data, *Buehler and Shearer* [2013] calculated the *Sn* propagation efficiency and identified highly attenuating regions in the western United States. Another strategy involves building a geometric spreading model followed by separating the attenuation from the spreading. *Yang et al.* [2007] proposed a log-quadratic geometric spreading function based on numerical simulations in a radially symmetric Earth model. *Avants et al.* [2011] further discussed the contribution of scattering to this spreading model. Applying this log-quadratic spreading model to Eurasia data, *Yang* [2011] obtained a more reasonable *Pn Q* between distances of 200 and 1000 km and frequencies of 0.5 and 10.0 Hz.

Between 2006 and 2013, North Korea conducted three underground nuclear tests. Compared with natural earthquakes, these explosive sources have accurate epicenter locations and source depths, simple and approximately identical source time functions, and most importantly virtually isotropic radiation patterns. Seismic networks recorded abundant regional phases from these events, including the *Pn* wave, in Northeast China, the Korean Peninsula, and Japan, across either the continental or the oceanic paths [e.g., *Chun et al.*, 2009; *Hong and Rhie*, 2009; *Murphy et al.*, 2013; *Richards and Kim*, 2007; *Wen and Long*, 2010; *Zhao et al.*, 2008, 2012, 2014].

In this study, we use this high-quality data set to investigate *Pn* wave propagation in Northeast China and the Korean Peninsula, including its geometrical spreading and the apparent *Pn* attenuation. An inversion method is used to formally separate the spreading and attenuation using the observed spectral amplitudes. Frequency-dependent parameters for a log-quadratic spreading model in Northeast China and the Korean Peninsula are derived from the data. Using two-station amplitude ratios and the known spreading function, we remove the effect of the crust leg from the apparent *Pn* wave attenuation to obtain the *P* wave attenuation along the pure upper mantle path. Combining both single-station amplitudes and two-station amplitude ratios, an uppermost mantle *P* wave attenuation tomography approach is proposed. Using *Pn* observations across Northeast China and those through the Japan Sea, the *Pn* spectral amplitudes across the continental and oceanic paths are compared.

2. Data

2.1. Regional Data Set

On 9 October 2006, 25 May 2009, and 12 February 2013, North Korea conducted three successive nuclear tests near the China-Korea border, and their body wave magnitudes were 4.2, 4.7, and 5.1, respectively, as reported by the United States Geological Survey (USGS). Hereafter, these events are referred to as NKT1, NKT2, and NKT3, and their parameters are provided in Table 1. Broadband digital seismograms from these nuclear tests are collected. Figure 1 depicts the locations of the North Korean nuclear test site (NKTS) and the 297 broadband stations used in this study. Among them, 188 permanent stations are from the national and provincial networks under the China Earthquake Administration and the China National Digital Seismic Network (CNDSN) operated by the China Earthquake Networks Center (CENC) since December 2000. Seven permanent stations are from the Global Seismographic Network (GSN), which has been operated by the

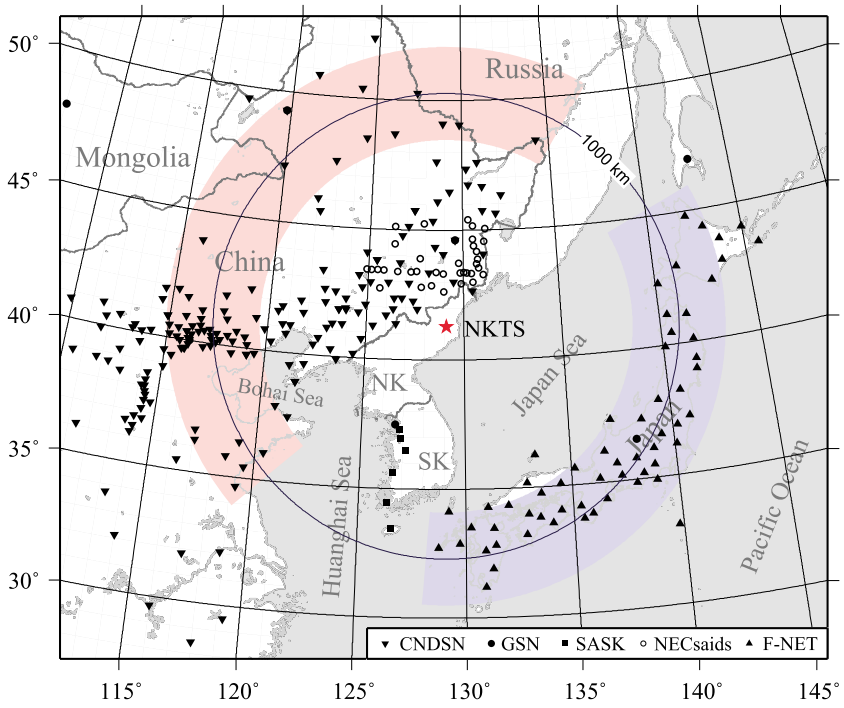

Figure 1. Map depicting locations of the North Korean test site (red star labeled NKTS) and seismic stations used in the study, including CNDSN (upset down triangles), GSN (solid circles), SASK (squares), NECsaids (open circles), and F-NET (triangles). The large circle indicates the 1000 km epicentral distance from the NKTS, with the pink and blue colors marking stations with continental and oceanic paths, respectively.

USGS and the Incorporated Research Institutions for Seismology (IRIS) consortium from May 1994 to present. Two portable seismic arrays, including the 6-station SASK in South Korea and the 35-station NECsaids in Northeast China, originally for investigating deep structures, recorded NKT2 and NKT3 with high signal-to-noise ratios. The remaining 61 stations are from F-NET in Japan. These stations are equipped with broadband instruments with nearly flat velocity responses between 0.03 and 8.0 Hz or wider, and their sampling rates vary among 20, 40, 50, and 100 points per second. The distances from the NKTS to these stations are between 143 and 1930 km, within which the *Pn* phase is well developed.

We plot regional waveforms in a record section to investigate the *Pn* wave group velocity in this area. Instead of plotting waveforms themselves, we plot normalized waveform energy. Figure 2a presents a vertical component velocity seismogram from NKT3 recorded by station LN.LYA at a distance of 813.0 km, where a band-pass filter between 0.1 and 10.0 Hz is applied. Figure 2b shows the normalized waveform energy. Figure 2c presents the waveform energy versus distance, in which several regional phases can be identified. The first arrival is the *Pn* wave, which has a group velocity of approximately 8.1 km/s. The *Pg* and *Lg* waves can be traced at group velocities of 6.0 and 3.5 km/s, respectively.

2.2. *Pn* Amplitude Measurements

The *Pn* wave is typically the first arrival at regional distances, and its amplitude can be measured within a time or group velocity window. For example, a fixed 5 s time window was used in Scandinavia by *Sereno et al.* [1988], a 4.3 s window was used in Eastern Canada by *Zhu et al.* [1991], and a 4.5 s window was used in Tibet by *Xie* [2007]. Considering the slightly dispersive properties of the *Pn* wave, some authors have used a group velocity window between 8.2 and 7.6 km/s to measure the amplitude [e.g., *Al-Damegh et al.*, 2004; *Mcnamara et al.*, 1997; *Reese et al.*, 1999]. In this study, we use the vertical component seismogram and a 0.7 km/s group velocity window around the IASP91 arrival time to measure the *Pn* amplitude. Figure 3 briefly illustrates the data processing process. The vertical component seismogram recorded at station LN.LYA from NKT3 is presented in Figure 3a, where the gray shaded areas indicate the 0.7 km/s group velocity window for measuring *Pn* and the pre-*P* arrival window for sampling the noise. The windowed signal is plotted in

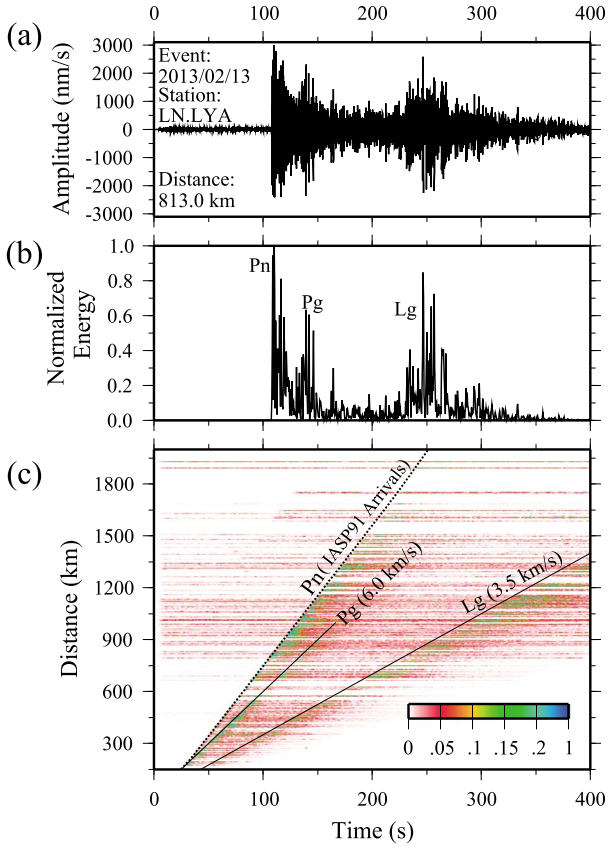

Figure 2. (a) A sample seismogram recorded at station LN.LYA, (b) its normalized energy, and (c) the record section of normalized waveform energy for all data used in this study. Color bar indicates the normalized energy level. The regional phases *Pn*, *Pg*, and *Lg* are labeled in Figures 2b and 2c.

Figure 3b, where 10% cosine tapers are applied at both ends. Following *Zhao et al.* [2010, 2013b], we select the noise series in an equal-length time window before the first arrival. Figure 3c presents the calculated Fourier spectra of the *Pn* and noise series between 0.3 and 15.0 Hz. The *Pn* spectral amplitudes are obtained at 44 frequencies distributed log-evenly between 0.3 and 15.0 Hz and corrected for the noise (Figures 3d and 3e). (for details, see *Zhao et al.* [2013a] and *Zhao et al.* [2010]).

3. *Pn* Wave Geometric Spreading and Attenuation

3.1. Modeling of the *Pn* Spectrum

The *Pn* wave spectrum can be expressed as [*Sereno et al.*, 1988; *Xie*, 2007; *Xie and Patton*, 1999]

$$A(f) = S(f)\cdot G(\Delta, f)\cdot \Gamma(\Delta, f)\cdot P(f)\cdot r(f), \tag{1}$$

where f is the frequency, $A(f)$ is the observed spectral amplitude, $P(f)$ is the site response, and $r(f)$ is the random amplitude effect. $S(f)$ is the *Pn* source spectrum, which is given by the following simplified explosion source function [*Hong*, 2013; *Mueller and Murphy*, 1971; *Sereno et al.*, 1988; *Xie and Patton*, 1999]:

$$S(f) = S_0\cdot\left[1 + (1-2\beta)\frac{f^2}{f_c^2} + \beta^2\frac{f^4}{f_c^4}\right]^{-1/2}, \tag{2}$$

where S_0 is the long period source spectral level, f_c is the corner frequency, and β controls the amount of overshot. For a Poisson medium, $\beta = 0.75$. For a near-surface explosion, $S_0 = M_0/4\pi\rho\alpha^3$, where M_0 is the seismic moment, and ρ and α are the density and P wave velocity in the source region [*Sereno et al.*, 1988; *Stevens and Day*, 1985], which in this study are set to 2.7 g/cm^3 and 5.5 km/s [*Hong et al.*, 2008; *Jih*, 1998], respectively. In equation (1), the geometric spreading factor $G(\Delta, f)$ is a function of the epicenter distance Δ and frequency f, and its details are provided in the next section. In equation (1),

$$\Gamma(\Delta, f) = \exp\left[-\frac{\pi f}{V}B(\Delta, f)\right] \tag{3}$$

is the attenuation factor, where V is the *Pn* wave group velocity, and will be treated as a regional constant,

$$B(\Delta, f) = \int_{\text{ray}}\frac{ds}{Q(f)} \tag{4}$$

is the integral of attenuation over the great circle path. In addition, $Q(f)$ is the apparent *Pn* wave Q and assumed can be expressed by a power law model [e.g., *Sereno et al.*, 1988; *Xie*, 2007]:

$$Q(f) = Q_0 f^{\eta}, \tag{5}$$

where Q_0 and η are the apparent *Pn* wave Q at 1 Hz and its frequency dependence, respectively.

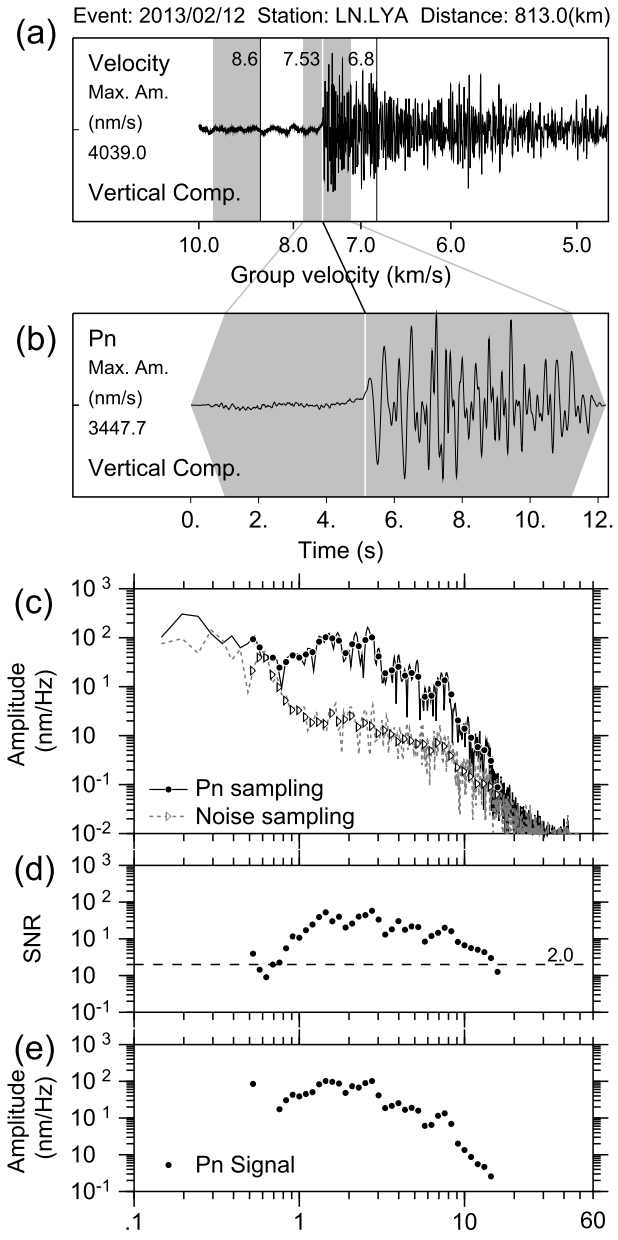

Figure 3. *Pn* wave spectral amplitude measurement. (a) Vertical component *Pn* seismogram, with the shaded areas indicating windows for *Pn* and the presignal noise, (b) *Pn* phase sampled by a 0.7 km/s group velocity window, (c) *Pn* wave and noise spectra, (d) signal-to-noise ratio (SNR), and (e) *Pn* spectra after noise correction. Note that the data samples for SNR < 2.0 are eliminated.

3.2. *Pn* Wave Geometric Spreading Function

The power law spreading function linearly relates the logarithmic amplitude with the logarithmic distance. To account for the complex spreading relation obtained from the *Pn* wave simulation in a spherical Earth, *Yang et al.* [2007] extended the power law relation by adding a second-order term. Considering that *Pn* spreading is frequency dependent, these researchers also included a quadratic form for its frequency dependency. We will call the model the log-quadratic spreading model, which exhibits the following form [*Yang et al.*, 2007]:

$$G(\Delta, f) = 10^{\xi_3(f)} \Delta^{\xi_1(f)\log_{10}\Delta - \xi_2(f)}, \quad (6)$$

where coefficients $\xi_n(f)$ are dependent on the logarithm of the frequency

$$\xi_n(f) = \xi_{n1}\log_{10}^2(f) + \xi_{n2}\log_{10}(f) + \xi_{n3}, \ (n = 1, 2, 3). \quad (7)$$

Based on a spherical Earth model composed of a 40 km thick crust and an underlying constant upper mantle, *Yang et al.* [2007] used numerical simulation to determine the coefficients as

$$\xi = \begin{bmatrix} -0.217 & 1.79 & 3.16 \\ -1.94 & 8.43 & 18.6 \\ -3.39 & 9.94 & 20.7 \end{bmatrix}. \quad (8)$$

Equation (6) is likely a more flexible model for the *Pn* geometric spreading than the simple power law model, but its coefficients can vary for regions with different velocities, crust thickness, and upper mantle lid structures. Therefore, we adopt equation (6) for Northeast China and the Korean Peninsula but fine tune its parameters using observed *Pn* data.

3.2.1. Prior Information and Model Space

Table 2 summarizes the model parameters to be searched for, including four parameters for sources, nine geometric spreading coefficients, and two parameters for the apparent *Pn* wave *Q*. We estimate the variation range of these parameters. For the three North Korean nuclear tests, their seismic moment M_0 and the corner frequency f_c can be calculated from their body wave magnitude m_b using the empirical relationship established by *Taylor et al.* [2002]. We set ±10% perturbations for m_b to obtain the variation ranges for M_0. The source corner frequency f_c can be calculated from the seismic moment using the empirical relation $\log M_0 = a + b \cdot \log f_c$ from *Xie and Patton* [1999]. From the *Pn* data recorded for explosions in central Asia, these researchers found $a = 18.34$ and $b = 4.73$. There is likely a trade-off between M_0 and a, so we fix

Table 2. Model Parameters of *Pn* Spectral Amplitude Used in This Study

	Model Space and Prior Information					Best Fit Inverted Model
	Parameter	Name	Prior Information	Data Range	Reference	(2.0–10.0 Hz)
Source		Seismic moment for				
	$M_0(N \cdot m)$	2013/02/13	2.0E + 16	$5.0E+15 \le M_0 \le 1.0E+17$	*Taylor et al.* [2002]	(7.133 ± 1.409)E + 15
		2009/05/25	3.0E + 15	$6.0E+14 \le M_0 \le 5.0E+15$		(4.015 ± 0.591)E + 15
		2006/10/09	4.0E + 14	$1.0E+14 \le M_0 \le 6.0E+14$		(5.080 ± 0.663)E + 14
	b	Slope for $\log M_0$-$\log f_c$ relation	4.73	$3.5 \le b \le 5.5$	*Xie and Patton* [1999]	5.112 ± 0.329
Geometric Spreading	ξ_{11}	Coefficient for *Pn* spreading	−0.217	$-0.239 \le \xi_{11} \le -0.195$	*Yang et al.* [2007]	−0.213 ± 0.010
	ξ_{12}		1.79	$1.611 \le \xi_{12} \le 1.969$		1.789 ± 0.089
	ξ_{13}		3.16	$2.844 \le \xi_{13} \le 3.476$		3.114 ± 0.131
	ξ_{21}		−1.94	$-2.134 \le \xi_{21} \le -1.746$		−1.993 ± 0.102
	ξ_{22}		8.43	$7.587 \le \xi_{22} \le 9.273$		8.459 ± 0.378
	ξ_{23}		18.6	$16.74 \le \xi_{23} \le 20.46$		18.328 ± 0.625
	ξ_{31}		−3.39	$-3.279 \le \xi_{31} \le -3.051$		−3.407 ± 0.183
	ξ_{32}		9.94	$8.946 \le \xi_{32} \le 10.934$		9.787 ± 0.509
	ξ_{33}		20.7	$18.63 \le \xi_{33} \le 22.77$		20.527 ± 0.916
Apparent Q Model	Q_0	1 Hz Q	204–325	$200 \le Q_0 \le 600$	e.g., *Xie* [2007] and *Yang* [2011]	237 (194 − 290)
	η	Frequency dependence	0.14–0.74	$-0.2 \le \eta \le 1.2$		0.361 ± 0.071

$a = 18.34$ in our model. The slope b also exhibits certain regional dependence, so we allow ± 30% variation for this parameter. The log-quadratic *Pn* spreading model derived by *Yang et al.* [2007] is expected to be transferable to other regions with proper modification of its parameters. Thus, we impose ±10% perturbation for all nine coefficients. *Sereno et al.* [1988] obtained apparent attenuation of $Q(f) = 325f^{0.48}$ in Scandinavia using 1 to 15 Hz *Pn* spectra. *Sereno* [1990] investigated *Pn* amplitude spectra in eastern Kazakhstan in central Asia and obtained a similar power law Q model of $Q(f) = 300f^{0.5}$. *Chun et al.* [1989] suggested that a frequency-dependent Q model, $Q(f) = 255f^{0.74}$, can explain the observed *Pn* spectra in the Canadian shield between 3 and 10 Hz. *Xie* [2007] used 0.6 to 5.0 Hz *Pn* spectra to obtain an average Q model, $Q(f) = 278f^{0.14}$, for the Tibetan Plateau. *Yang* [2011] investigated *Pn* geometric spreading based on observations in Asia, wherein he observed that the *Pn* Q approximately follows a power law function $Q(f) = 204f^{0.58}$ for frequencies greater than 2 Hz. Using these results as prior information, we limit the range of Q_0 and η from 200 to 600 and from −0.2 to 1.2, respectively. All prior information and model parameter spaces are summarized in Table 2.

3.2.2. *Pn* Geometric Spreading Model in Northeast China and the Korean Peninsula

Because of the potentially different *Pn* propagation characteristics of continental and oceanic paths and because the continental data set covers a wide and relatively even distance range, we use only continental path *Pn* amplitude measurements in the following parameter searching and tomography analysis. We also restrict our analysis to amplitudes within 2.0 to 10.0 Hz due to apparently different *Pn* attenuation behavior (see Figure 7d) beyond this frequency range. Simulated annealing [*Kirkpatrick et al.*, 1983], a nonexhaustive global optimization algorithm, is used to estimate the parameters in model space. This method has been widely applied in geophysical modeling [e.g., *Iritani et al.*, 2014; *Kirkpatrick*, 1984; *Zhao et al.*, 1996]. We perform the parameter searching by minimizing the L2 norm misfit function of the difference between observed and synthetic *Pn* amplitudes. Figure 4 illustrates the *Pn* spectral amplitudes at selected frequencies, after correcting for the source excitation functions. Different symbols indicate that the samples are from NKT1 (triangles), NKT2 (circles), and NKT3 (crosses). The solid blue lines are the best fit *Pn* amplitudes from data between 2.0 and 10.0 Hz, and the shaded areas are their standard deviations of the fit calculated using the bootstrap method [*Efron*, 1983]. The frequency f, number of samples N, apparent regional average *Pn* Q, and correlation coefficient R are labeled in each panel.

The inverted *Pn* models are listed in Table 2 and illustrated in Figure 5. Figures 5a and 5b presents the *Pn* geometric spreading curves versus distance at 2.1 and 9.1 Hz, respectively. Figures 5c and 5d present these curves versus frequency at distances of 500 and 1200 km, respectively. The solid lines indicate the results

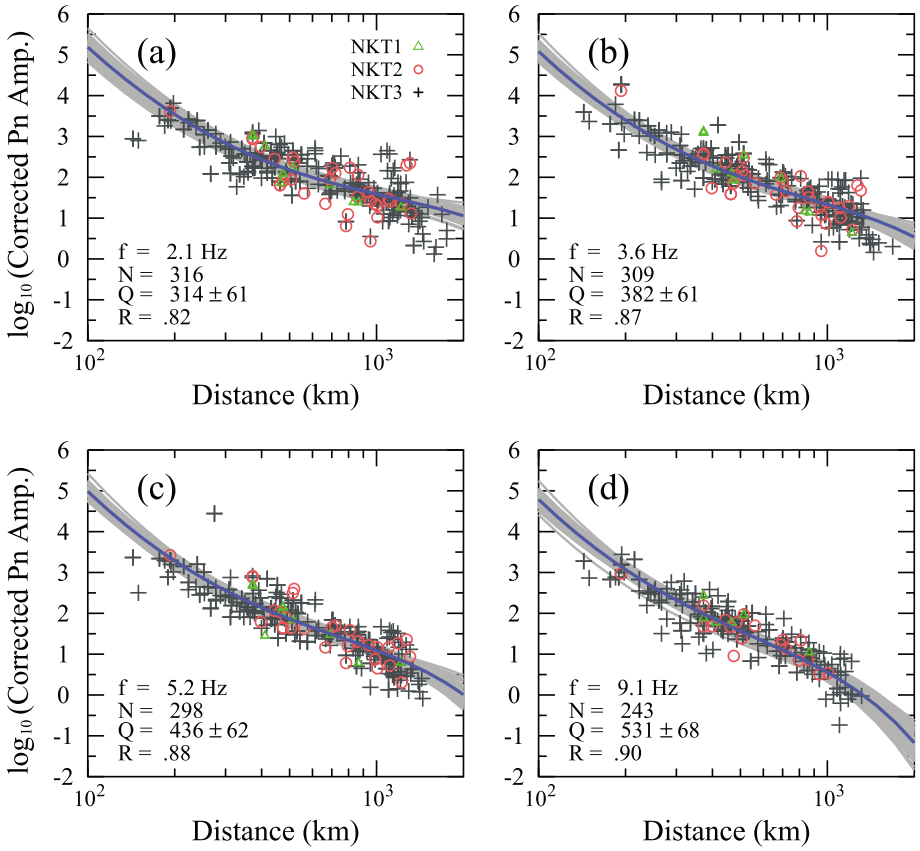

Figure 4. *Pn* spectral amplitudes versus distance at selected frequencies. The source excitation spectra have been removed. Different symbols indicate data from NKT1 (triangles), NKT2 (circles), and NKT3 (crosses). The solid blue lines are the best fit *Pn* spectra with data between 2.0 and 10.0 Hz, and the shaded areas represent their standard deviations. The frequency (f), number of samples (N), apparent *Pn* Q, and correlation coefficient (R) are labeled in each panel.

obtained here, and the dashed lines represent the model proposed by *Yang et al.* [2007]. The two spreading models exhibit similar overall shapes that first decrease and then increase with increasing distance. The minimums appear at shorter distances for higher frequencies. The models are also positively frequency dependent, at least within the investigated frequency band. Figure 5e illustrates the inverted source excitation functions, where the shaded areas are the standard deviations. Figure 5f presents the average regional *Pn* Q versus the frequency.

4. Upper Mantle *P* Wave Attenuation

Pn wave attenuation is an apparent value because the *Pn* Q observed along the great circle is mixed with those traveling in the uppermost mantle and crust, with the latter propagating with a nonzero dipping angle. With the known *Pn* wave geometric spreading function, we can remove the effect of crust legs and obtain the upper mantle *P* wave attenuation.

4.1. Single-Station Data

Figure 6 presents the *Pn* propagation path between the NKTS and station LN.LYA, calculated using the CRUST1.0 model [*Laske et al.*, 2013]. The refraction points E and F separate the raypath into three sections, including the crust leg at the source side, the uppermost mantle leg, and the crust leg at the station side. From equation (4), $B(\Delta, f)$ can be expressed as

$$B(\Delta, f) = \int_{AE} \frac{ds}{Q_s} + \int_{EF} \frac{ds}{Q(x, y, f)} + \int_{FB} \frac{ds}{Q_r}, \tag{9}$$

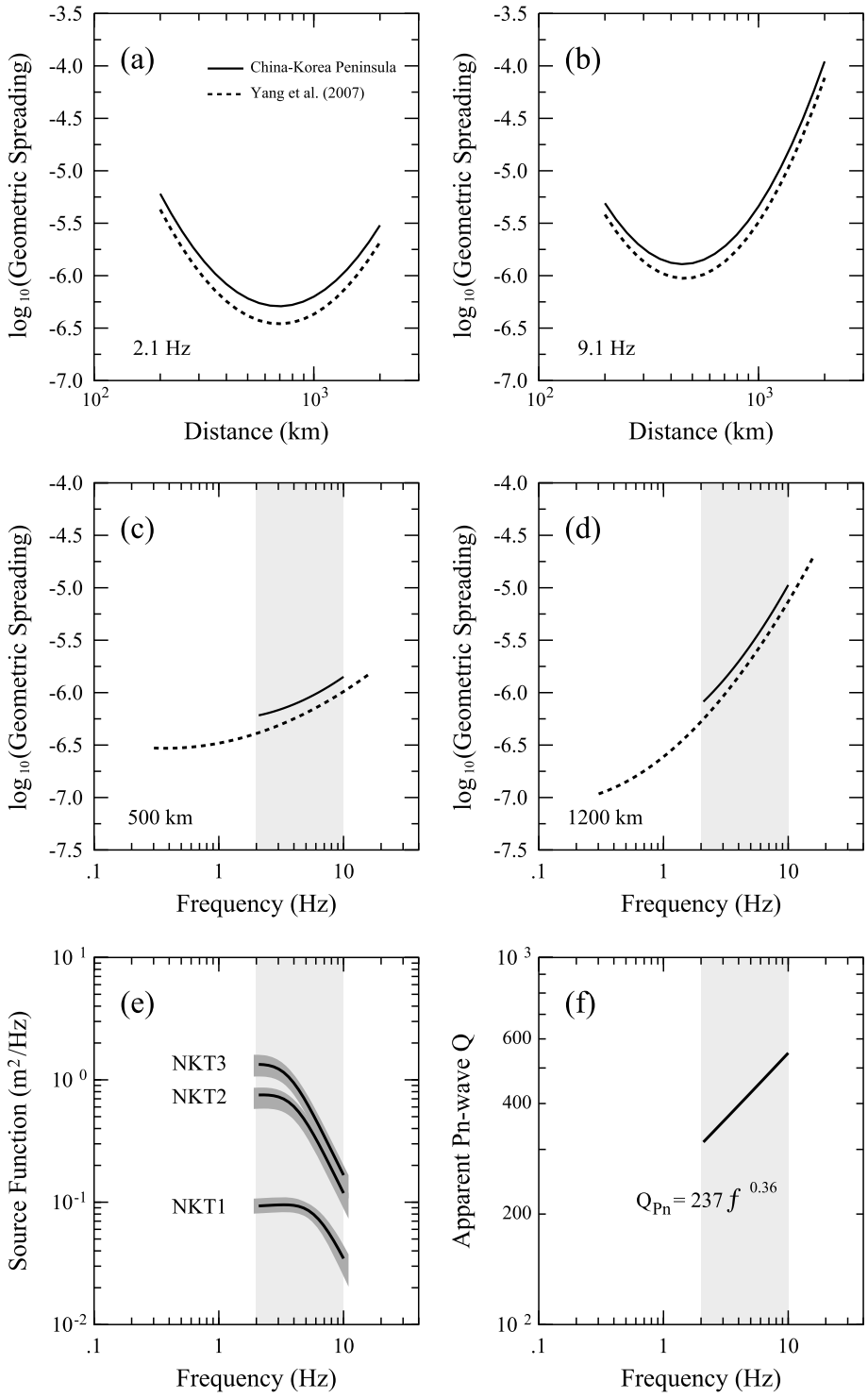

Figure 5. The inverted *Pn* models. (a and b) The *Pn* geometric spreading functions versus distance at 2.1 and 9.1 Hz. (c and d) The *Pn* geometric spreading functions versus frequency at 500 and 1200 km. (e) Source excitation functions for three nuclear explosions and (f) regional average *Pn Q* versus frequency. The solid lines are the result for Northeast China and the Korean Peninsula obtained using 2.0 to 10.0 Hz data, and the dashed lines represent the model given by *Yang et al.* [2007].

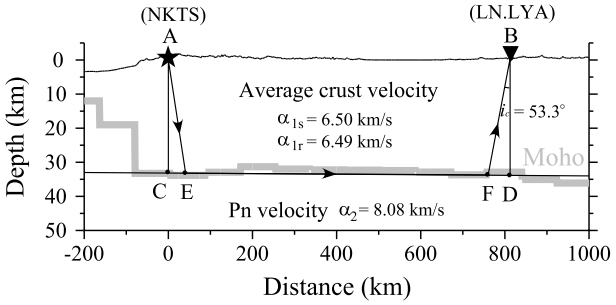

Figure 6. Sketch depicting the *Pn* wave propagation path from the NKTS to LN.LYA. The crust model is based on CRUST1.0.

where Q_s and Q_r are the source and station side crust *P* wave *Q*, and $Q(x, y, f)$ is the uppermost mantle *P* wave *Q*, which is a function of the frequency and location (x, y) between *E* and *F*. By substituting equation (9) into (3), the *Pn* attenuation factor can be expressed as

$$\begin{aligned}\Gamma(\Delta, f) &= \Gamma_s(AE, f)\cdot\Gamma(EF, f)\cdot\Gamma_r(FB, f)\\ &= \exp\left[-\frac{\pi f}{\alpha_{1s}}\int_{AE}\frac{ds}{Q_s}-\frac{\pi f}{\alpha_2}\int_{EF}\frac{ds}{Q(x,y,f)}-\frac{\pi f}{\alpha_{1r}}\int_{FB}\frac{ds}{Q_r}\right],\end{aligned} \tag{10}$$

where α_{1s} and α_{1r} are the source and station side *P* wave velocity, α_2 is the upper mantle *P* wave velocity. From equations (1) and (10), we have

$$A(f)G^{-1}(\Delta, f)\cdot S^{-1}(f) = [\Gamma_s(AE, f)\Gamma_r(FB, f)]\cdot\exp\left[-\frac{\pi f}{\alpha_2}\int_{EF}\frac{ds}{Q(x,y,f)}\right], \tag{11}$$

where $G(\Delta, f)$ and $S(f)$ are known from section 3 and $A(f)G^{-1}(\Delta, f)\cdot S^{-1}(f)$ is the spreading and source corrected single-station data. $\Gamma_s(AE, f)\cdot\Gamma_r(FB, f)$ is the attenuation from the crust legs. We assume that it is an unknown constant over the studied region and can be inverted for from the data. It is expected that the upper mantle leg dominates the *Pn* propagation, and the error in the crust legs can be neglected. We will also neglect factors $P(f)$ and $r(f)$ caused by the site effect and the random fluctuations.

4.2. Two-Station Data and *Pn* Amplitude Ratio

Assuming that the two stations are located at different epicenter distances but within the similar azimuth direction from the NKTS, we calculate their amplitude ratio as follows [e.g., *Xie et al.*, 2004]:

$$A_{ij} = \frac{A_j(f)}{A_i(f)} = \frac{G(\Delta_j, f)}{G(\Delta_i, f)}\frac{\Gamma_s(AE_j, f)}{\Gamma_s(AE_i, f)}\frac{\Gamma(EF_j, f)}{\Gamma(EF_i, f)}\frac{\Gamma_r(FB_j, f)}{\Gamma_r(FB_i, f)}\frac{P_j(f)\cdot r_j(f)}{P_i(f)\cdot r_i(f)}, \tag{12}$$

where $A_i(f)$ and $A_j(f)$ are the *Pn* amplitude spectra observed at stations *i* and *j*, the source terms have been canceled, and $G(\Delta_j, f)/G(\Delta_i, f)$ is the ratio between known geometrical spreading functions at these distances. $\Gamma_s(AE_i, f)$ and $\Gamma_s(AE_j, f)$ represent the source side crust legs. For observations from the same source, their ratio should be equal to unity. $\Gamma_r(FB_i, f)$ and $\Gamma_r(FB_j, f)$ represent the station side crust legs. As above mentioned, we assume these values are approximately the same, and their ratio approaches unity. We also neglect the ratio $P_j(f)\cdot r_j(f)/P_i(f)\cdot r_i(f)$. After these treatments and by introducing equation (10), equation (12) becomes

$$A_{ij}(f)\frac{G(\Delta_i, f)}{G(\Delta_j, f)} = \exp\left[-\frac{\pi f}{\alpha_2}\int_{F_i}^{F_j}\frac{ds}{Q(x,y,f)}\right], \tag{13}$$

where the integral $\int_{F_i}^{F_j} 1/Q(x, y, f)ds$ is from the refraction point F_i to F_j over the upper mantle path. The left hand side of equation (13), the amplitude ratio corrected by the known geometrical spreading function, is directly linked to the accumulated attenuation over the pure upper mantle path. Thus, the two-station amplitude ratio removes the source term and contributions from the crust legs near the source and station.

Figures 7a–7c illustrate the *Pn* amplitude ratios after correction for the spreading function versus the interstation distance at 3.0, 5.2, and 9.1 Hz. The solid lines are linear regressions, and their slopes provide the regional average upper mantle *P* wave *Q*. The circles in Figure 7d represent upper mantle *P* wave *Q* versus frequency. They show a nearly linear relation between 2.0 and 10.0 Hz (shaded area), within which a power law *Q* model,

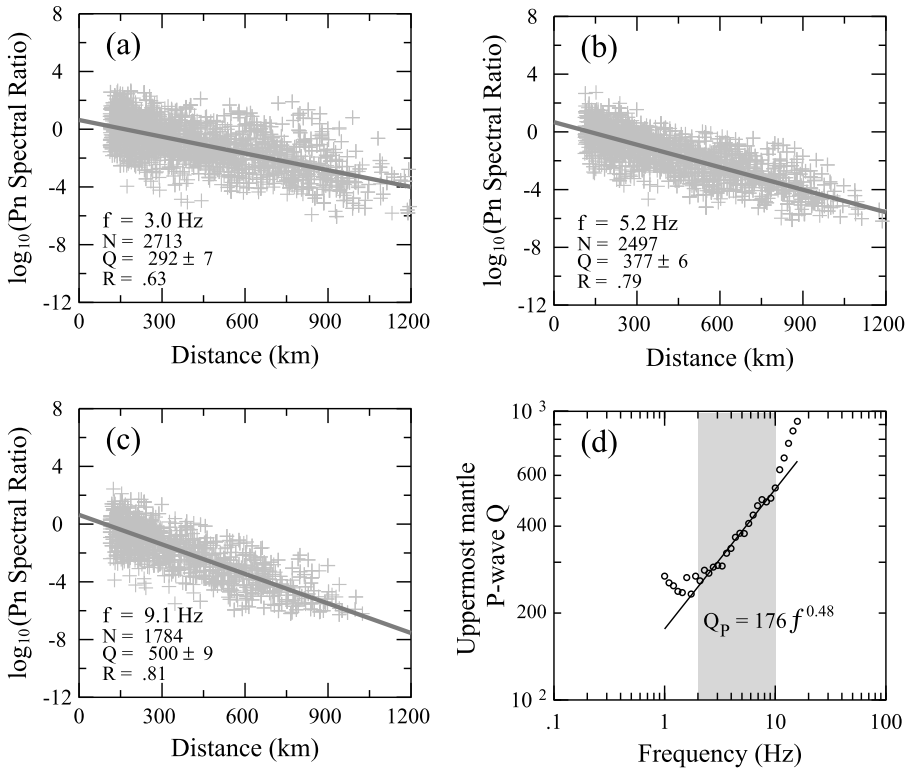

Figure 7. (a–c) Spreading-corrected *Pn* spectral ratios (light gray crosses) versus interstation distance at 3.0, 5.2, and 9.1 Hz. The solid lines indicate linear regressions, and their slopes represent the regional average uppermost mantle *P* wave *Q*. (d) Regional average uppermost mantle *P* wave *Q* (circles) versus frequencies. The solid line is the best fit power law *Q* model using data between 2.0 and 10.0 Hz.

$Q_P = 176f^{0.48}$, for the upper mantle *P* wave can be obtained. However, outside this frequency band, the *Q* versus frequency behaves quite differently. In our *Pn Q* model, we assume a power law frequency dependence. The results demonstrate that this assumption may only be valid within the 2.0 to 10.0 Hz band in the studied region.

4.3. Upper Mantle *P* Wave *Q* Tomography

An inversion system for the upper mantle *P* wave *Q* can be created either from the single-station data, the two-station data, or by combining both. One might think that the two data sets are from the same group of observations and should contain exactly the same information, but certain differences still exist. The advantage of using the two-station data is that the amplitude ratio eliminates the source effect at the data processing stage, reducing the tradeoff between the source term and attenuation in the inversion. However, the slight azimuth difference between two stations may result in additional errors. Most importantly, the two-station data must match the source-station geometry, which often results in less useful rays and shorter ray length compared with the single-station method. This effect is particularly severe for the heavily attenuated region and for high frequencies, where near-station information is vital. Thus, combining the single- and two-station data improves data coverage and avoids serious tradeoffs.

Similar to the *Lg* wave *Q* tomography [e.g., *Zhao et al.*, 2010, 2013b], we linearize equations (11) and (13) by taking the logarithm to combine both the single- and the two-station data for inversion. In our tomography, the initial *Q* model is a constant model resulted from two-station data analysis, as shown in Figure 7. The same constant *Q* model is also used to create checkerboard model for resolution testing. A broadband uppermost mantle *P* wave attenuation model in Northeast China and the Korean Peninsula at 18 discrete frequencies between 2.0 and 10.0 Hz is obtained. As examples, Figure 8a presents the *P* wave *Q* distribution at 3.0 Hz, and Figure 8b presents the broadband *Q*, which is calculated by average logarithmic *Q* between 2.0 and 10.0 Hz. The major geology blocks, including the Songliao Basin (SB), Bohai Bay Basin (BB), and Changbai

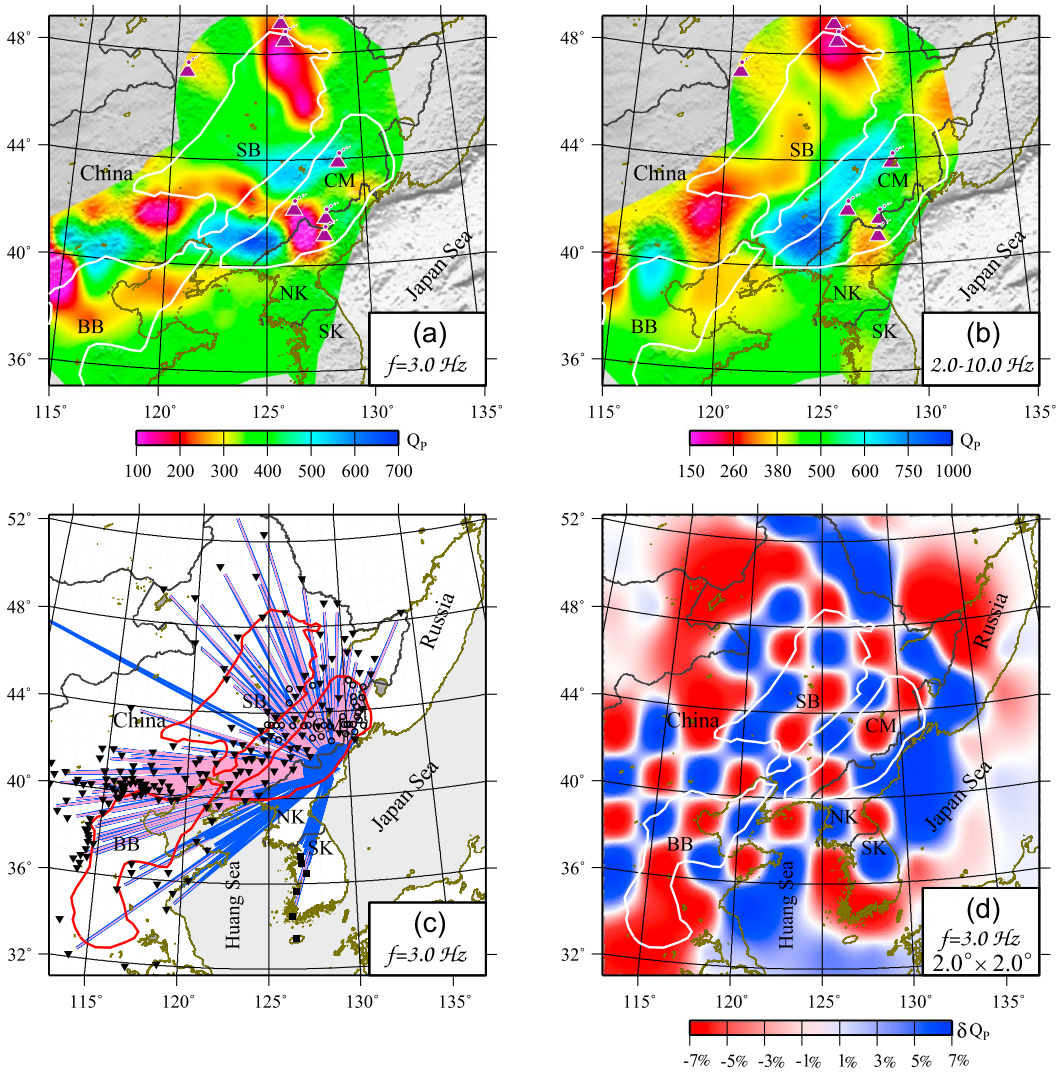

Figure 8. Results for the upper mantle *P* wave *Q* model. (a) Inverted *Q* map at 3.0 Hz, (b) the broadband *Q* obtained by averaging logarithmic *Q* between 2.0 and 10.0 Hz, (c) 3 Hz raypath coverage, in which the blue and pink lines indicate the single- and two-station paths, respectively, and (d) 2.0° × 2.0° checkerboard test for 3 Hz resolution check.

Mountains (CM), are illustrated in these figures. The northern SB, the areas between the southern SB and BB, and the southeastern CM are characterized by low *Q* anomalies, whereas areas between SB and CM are high *Q* regions. A number of volcanoes in this region were previously investigated using seismic velocity tomography [e.g., *Duan et al.*, 2009; *Lei and Zhao*, 2005; *Zhao et al.*, 2009, 2011]. Prominent low *P* wave velocity anomalies have been found in the crust and upper mantle beneath these volcanoes [*Zhao et al.*, 2009]. These anomalies are consistent with the strong *P* wave attenuation in the uppermost mantle observed in this study. Figures 8c and 8d illustrate the 3.0 Hz ray coverage and the checkerboard test for the 2.0° × 2.0° resolution.

5. Comparison of *Pn* Wave Amplitudes Through Continental and Oceanic Paths

The ray paths from NKTS to Japan cross the Japan Sea, where the oceanic Moho depth is approximately 11 to 15 km [*Laske et al.*, 2013]. The continental crust and oceanic crust have different thicknesses and underlying upper mantle *P* wave velocities, and the transition zone between them may also influence *Pn* attenuation and spreading. In Figure 1, the data observed via continental path surround the NKTS for an azimuth range of approximately 160° and cover epicenter distances from 150 to 1300 km, forming the data set for investigating the *Pn* spreading function and attenuation in Northeast China and the Korean Peninsula. The data crossing

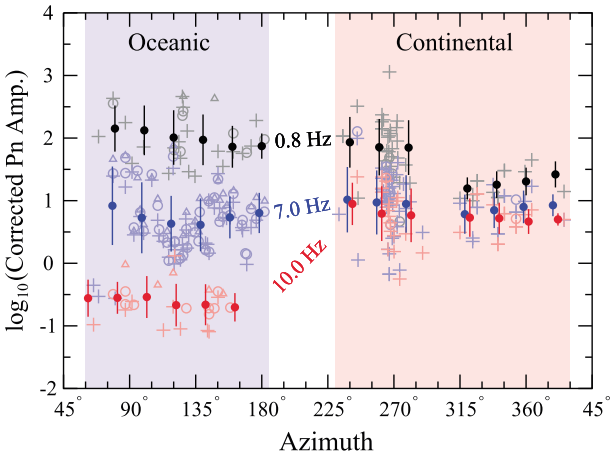

Figure 9. *Pn* spectral amplitudes at distance 1000 km versus the azimuth. The triangles, circles, and crosses represent NKT1, NKT2, and NKT3, respectively. Black, blue, and red colors indicate 0.8, 7.0, and 10.0 Hz data, respectively. Solid circles with error bars represent their mean values and standard deviations, obtained within 30° azimuth windows. The *Pn* source excitation functions are removed from the data.

the oceanic path are mostly recorded by F-NET stations in Japan. The data cover an azimuth range of approximately 120° but are mostly recorded at distances of approximately 1000 km, thus preventing them from being used for an independent geometric spreading function for the oceanic path.

Given that the explosion sources are virtually isotropic and the observations are nearly completely surrounding the source, the data still provide an excellent opportunity to investigate the *Pn* amplitudes and their frequency dependency on the continental and oceanic paths. To avoid ambiguity, we make a straight forward comparison with minimum data processing. Given that the oceanic data are mostly recorded at 1000 km, we collect the *Pn* spectral amplitudes between distances 800 and 1200 km (with a nominal epicentral distance of 1000 km). We remove the *Pn* wave source excitation functions and present the result in Figure 9 as a function of the azimuth. The triangles, circles, and crosses are the directly measured spectral amplitudes for NKT1, NKT2, and NKT3. In addition, black, blue, and red colors indicate 0.8, 7.0, and 10.0 Hz data, respectively. Solid circles with error bars indicate the mean values and standard deviations obtained within a 30° azimuth window. Prominent differences can be observed for the *Pn* waves crossing different paths. Between 60° and 180°, the *Pn* signals crossing the oceanic path are strongly frequency dependent, with extremely low high-frequency amplitudes. The *Pn* waves across the continental path can be divided into two groups. Between 230° and 280° with the direction toward Northern China, the low-frequency contents (0.8 and 7.0 Hz) are similar to that from the oceanic path, but the high-frequency (10.0 Hz) propagation is much more efficient than that from the oceanic path. Within the azimuth range of 315° to 30° toward Northeast China, the *Pn* spectra are less dependent on the frequency. In general, the intermediate frequency (7.0 Hz) spectra are less affected by different paths, but the low- and high-frequency contents exhibit apparent variations between the continental and oceanic paths. Because no data processing, other than the noise and source excitation function removal is involved, the observations are relatively reliable. The spreading function tends to raise the high-frequency signal, whereas attenuation tends to reduce the high-frequency contents. The detailed structure of transition zones may also affect the frequency dependence. Additional observational and/or numerical investigations are required to distinguish contributions from individual mechanisms.

6. Discussion

To determine the *Pn* wave geometric spreading function and the attenuation, several assumptions are adopted, e.g., isotropic source radiation, a log-quadratic spreading model, and a power law *Pn Q* model. Given that both geometric spreading and attenuation are frequency dependent, trade-offs between them may exist. Certain clues (e.g., Figure 7d) indicate that a power law *Q* model may oversimplify the frequency dependency of the attenuation in a broad frequency band. In section 3, we obtain the regional average *Pn Q* using the single-station data, and we obtain the regional average upper mantle *P* wave *Q* using the two-station data in section 4. However, because the single-station data extend to a larger region compared with the two-station data, the two average *Q*s do not necessarily cover the same region. In the upper mantle *P* wave attenuation tomography, all seismic rays come from the same epicenter and there are no crossing rays. This forms an unfavorable geometry for a high-quality tomography. Therefore, the result is limited and primarily used for introducing the technique.

The *Pn* wave has a typical group velocity window between 8.2 and 7.6 km/s for continental paths. Selecting a window and the component to measure the *Pn* spectra is an important issue. *Sereno et al.* [1988] tested different window lengths of 5 to 20 s and suggested that the spectra are insensitive to the window length. In fact, their shortest 5 s window generated approximately the same *Pn* measurements for low-magnitude earthquakes with epicentral distances between 200 and 1400 km. To investigate the stability of the *Pn* wave amplitude measurement, we tested four different methods, including combinations from two different *Pn* wave windows (a 0.7 km/s group velocity window around the IASP91 arrival times and a fixed 4 s window after the first arriving *P* wave) and two different displacement components (vertical component and the displacement rotated to the *Pn* incident direction). The methods generally exhibit consistent results. Therefore, we only present the result from the vertical component and a 0.7 km/s group velocity window.

7. Conclusions

We present a method to separate the geometric spreading and attenuation from the seismic *Pn* wave data. The frequency-dependent, log-quadratic spreading function of *Yang et al.* [2007] and the power law *Q* model are adopted for *Pn* propagation. A high-accuracy broadband *Pn* wave data set from the recent North Korean nuclear explosions is used to constrain the model parameters. The geometric spreading function and regional *Pn Q* are obtained for Northeast China and the Korean Peninsula. By taking the two-station amplitude ratios and correcting for the known spreading function, we remove the effects of the source and crust legs from *Pn* data, obtaining the *P* wave attenuation information along the pure upper mantle path. Combining both the single- and the two-station data, the upper mantle *P* wave attenuation distribution is obtained using a formal tomographic approach. The current method can be applied to earthquake data as well as *Sn* waves. We compared the *Pn* waves across China and through the Japan Sea. The results reveal prominent differences for *Pn* waves crossing different paths, with the high-frequency *Pn* signal propagating more efficiently through the continental path compared with the oceanic path.

Acknowledgments

The comments from Thomas M. Hearn and another anonymous reviewer are valuable and greatly improved this manuscript. This research was supported by the National Natural Science Foundation of China (grants 41174048, 41374065, 41130316, 4062140435, and 41210005). X.B. Xie wishes to thank AFRL for support under grant FA9453-12-C-0234. The waveforms recorded at the CNDSN, GSN, and F-NET stations used in this study were collected from the China Earthquake Network Center (CENC), the Data Management Centre of the China National Seismic Network at the Institute of Geophysics, the China Earthquake Administration (SEISDMC, doi:10.7914/SN/CB) [*Zheng et al.*, 2010], the Incorporated Research Institutions for Seismology Data Management Center (IRIS DMC) at www.iris.edu (last accessed April 2015), and the National Research Institute for Earth Science and Disaster Prevention (NIED) at http://www.fnet.bosai.go.jp (last accessed April 2015). The seismograms recorded at the SASK and NECsaids stations were provided by the Seismic Array Laboratory (SAL) at the Institute of Geology and Geophysics, Chinese Academy of Sciences (IGGCAS). Some of the figures were generated using the Generic Mapping Tools version 4.3.1 (www.soest.hawaii.edu/gmt, last accessed April 2015) [*Wessel and Smith*, 1998].

References

Al-Damegh, K., E. Sandvol, A. Al-Lazki, and M. Barazangi (2004), Regional seismic wave propagation (Lg and Sn) and Pn attenuation in the Arabian plate and surrounding regions, *Geophys. J. Int.*, *157*(2), 775–795, doi:10.1111/j.1365-246X.2004.02246.x.

Avants, M., T. Lay, X. B. Xie, and X. N. Yang (2011), Effects of 2D random velocity heterogeneities in the mantle lid and Moho topography on P_n geometric spreading, *Bull. Seismol. Soc. Am.*, *101*(1), 126–140, doi:10.1785/0120100113.

Barron, J., and K. Priestley (2009), Observations of frequency-dependent S_n propagation in Northern Tibet, *Geophys. J. Int.*, *179*(1), 475–488, doi:10.1111/j.1365-246X.2009.04318.x.

Buehler, J. S., and P. M. Shearer (2013), *Sn* propagation in the Western United States from common midpoint stacks of USArray data, *Geophys. Res. Lett.*, *40*, 6106–6111, doi:10.1002/2013GL057680.

Calvert, A., E. Sandvol, D. Seber, M. Barazangi, F. Vidal, G. Alguacil, and N. Jabour (2000), Propagation of regional seismic phases (Lg and Sn) and Pn velocity structure along the Africa-Iberia plate boundary zone: Tectonic implications, *Geophys. J. Int.*, *142*(2), 384–408, doi:10.1046/j.1365-246x.2000.00160.x.

Červený, V., and R. Ravindra (1971), *Theory of Seismic Head Waves*, 312 pp., Univ. of Toronto Press, Toronto, Ontario.

Chun, K. Y., R. J. Kokoski, and G. F. West (1989), High-frequency *Pn* attenuation in the Canadian shield, *Bull. Seismol. Soc. Am.*, *79*(4), 1039–1053.

Chun, K. Y., Y. Wu, and G. A. Henderson (2009), *Lg* attenuation near the North Korean border with China, Part I: Model development from regional earthquake sources, *Bull. Seismol. Soc. Am.*, *99*(5), 3021–3029, doi:10.1785/0120080316.

Duan, Y. H., D. P. Zhao, X. K. Zhang, S. H. Xia, Z. Liu, F. Y. Wang, and L. Li (2009), Seismic structure and origin of active intraplate volcanoes in Northeast Asia, *Tectonophysics*, *470*(3–4), 257–266, doi:10.1016/j.tecto.2009.01.004.

Efron, B. (1983), Estimating the error rate of a prediction rule: Improvement on cross-validation, *J. Am. Stat. Assoc.*, *78*(382), 316–331, doi:10.2307/2288636.

Hill, D. P. (1973), Critically refracted waves in a spherically symmetric radially heterogeneous Earth model, *Geophys. J. R. Astron. Soc.*, *34*(2), 149–177, doi:10.1111/j.1365-246X.1973.tb02390.x.

Hong, T. K. (2013), Seismic discrimination of the 2009 North Korean nuclear explosion based on regional source spectra, *J. Seismol.*, *17*(2), 753–769, doi:10.1007/s10950-012-9352-1.

Hong, T. K., and J. Rhie (2009), Regional source scaling of the 9 October 2006 underground nuclear explosion in North Korea, *Bull. Seismol. Soc. Am.*, *99*(4), 2523–2540, doi:10.1785/0120080007.

Hong, T. K., C. E. Baag, H. Choi, and D. H. Sheen (2008), Regional seismic observations of the 9 October 2006 underground nuclear explosion in North Korea and the influence of crustal structure on regional phases, *J. Geophys. Res.*, *113*, B03305, doi:10.1029/2007JB004950.

Iritani, R., N. Takeuchi, and H. Kawakatsu (2014), Intricate heterogeneous structures of the top 300 km of the Earth's inner core inferred from global array data: II. Frequency dependence of inner core attenuation and its implication, *Earth Planet. Sci. Lett.*, *405*, 231–243, doi:10.1016/j.epsl.2014.08.038.

Jih, R. S. (1998), Location calibration effects in China, in *Proceedings, 20th Annual Seismic Research Symposium on Monitoring a Comprehensive Test Ban Treaty*, pp. 44–45, Santa Fe, New Mexico.

Kirkpatrick, S. (1984), Optimization by simulated annealing: Quantitative studies, *J. Stat. Phys.*, *34*(5–6), 975–986, doi:10.1007/Bf01009452.

Kirkpatrick, S., C. D. Gelatt, and M. P. Vecchi (1983), Optimization by simulated annealing, *Science*, *220*(4598), 671–680, doi:10.1126/science.220.4598.671.

Laske, G., G. Masters, Z. Ma, and M. Pasyanos (2013), Update on CRUST1.0—A 1-degree global model of Earth's crust, *Geophys. Res. Abstracts*, *15*, Abstract EGU2013-2658.

Lei, J. S., and D. P. Zhao (2005), P-wave tomography and origin of the Changbai intraplate volcano in Northeast Asia, *Tectonophysics*, *397*(3–4), 281–295, doi:10.1016/j.tecto.2004.12.009.

McNamara, D. E., W. R. Walter, T. J. Owens, and C. J. Ammon (1997), Upper mantle velocity structure beneath the Tibetan Plateau from Pn travel time tomography, *J. Geophys. Res.*, *102*(B1), 493–505, doi:10.1029/96JB02112.

Mueller, R. A., and J. R. Murphy (1971), Seismic characteristics of underground nuclear detonaions. Part I. Seismic spectrum scaling, *Bull. Seismol. Soc. Am.*, *61*(6), 1675–1692.

Murphy, J. R., J. L. Stevens, B. C. Kohl, and T. J. Bennett (2013), Advanced seismic analyses of the source characteristics of the 2006 and 2009 North Korean nuclear tests, *Bull. Seismol. Soc. Am.*, *103*(3), 1640–1661, doi:10.1785/0120120194.

Reese, C. C., R. R. Rapine, and J. F. Ni (1999), Lateral variation of *Pn* and *Lg* attenuation at the CDSN station LSA, *Bull. Seismol. Soc. Am.*, *89*(1), 325–330.

Richards, P. G., and W. Y. Kim (2007), Seismic signature, *Nat. Phys.*, *3*(1), 4–6, doi:10.1038/Nphys495.

Sereno, T. J. (1990), Frequency-dependent attenuation in Eastern Kazakhstan and implications for seismic detection thresholds in the Soviet Union, *Bull. Seismol. Soc. Am.*, *80*(6), 2089–2105.

Sereno, T. J., and J. W. Given (1990), *Pn* attenuation for a spherically symmetric Earth model, *Geophys. Res. Lett.*, *17*(8), 1141–1144, doi:10.1029/GL017i008p01141.

Sereno, T. J., S. R. Bratt, and T. C. Bache (1988), Simultaneous inversion of regional wave spectra for attenuation and seismic moment in Scandinavia, *J. Geophys. Res.*, *93*(B3), 2019–2035, doi:10.1029/JB093iB03p02019.

Stevens, J. L., and S. M. Day (1985), The physical basis of m_b: M_s and variable frequency magnitude methods for earthquake/explosion discrimination, *J. Geophys. Res.*, *90*(B4), 3009–3020, doi:10.1029/JB090ib04p03009.

Taylor, S. R., A. A. Velasco, H. E. Hartse, W. S. Phillips, W. R. Walter, and A. J. Rodgers (2002), Amplitude corrections for regional seismic discriminants, *Pure Appl. Geophys.*, *159*(4), 623–650.

Wen, L. X., and H. Long (2010), High-precision location of North Korea's 2009 nuclear test, *Seismol. Res. Lett.*, *81*(1), 26–29, doi:10.1785/gssrl.81.1.26.

Wessel, P., and W. Smith (1998), New, improved version of the Generic Mapping Tools released, *Eos Trans. AGU*, *79*, 579.

Xie, J. (2007), *Pn* attenuation beneath the Tibetan Plateau, *Bull. Seismol. Soc. Am.*, *97*(6), 2040–2052, doi:10.1785/0120070016.

Xie, J., and H. J. Patton (1999), Regional phase excitation and propagation in the Lop Nor region of central Asia and implications for P/Lg discriminants, *J. Geophys. Res.*, *104*(B1), 941–954, doi:10.1029/1998JB900045.

Xie, J., R. Gök, J. Ni, and Y. Aoki (2004), Lateral variations of crustal seismic attenuation along the INDEPTH profiles in Tibet from Lg Q inversion, *J. Geophys. Res.*, *109*, B10308, doi:10.1029/2004JB002988.

Yang, X. (2011), A Pn spreading model constrained with observed amplitudes in Asia, *Bull. Seismol. Soc. Am.*, *101*(5), 2201–2211, doi:10.1785/0120100314.

Yang, X., T. Lay, X. B. Xie, and M. S. Thorne (2007), Geometric spreading of Pn and Sn in a spherical Earth model, *Bull. Seismol. Soc. Am.*, *97*(6), 2053–2065, doi:10.1785/0120070031.

Zhao, D. P., Y. Tian, J. S. Lei, L. C. Liu, and S. H. Zheng (2009), Seismic image and origin of the Changbai intraplate volcano in East Asia: Role of big mantle wedge above the stagnant Pacific slab, *Phys. Earth Planet. Inter.*, *173*(3–4), 197–206, doi:10.1016/j.pepi.2008.11.009.

Zhao, D. P., S. Yu, and E. Ohtani (2011), East Asia: Seismotectonics, magmatism and mantle dynamics, *J. Asian Earth Sci.*, *40*(3), 689–709, doi:10.1016/j.jseaes.2010.11.013.

Zhao, L. F., X. B. Xie, W. M. Wang, and Z. X. Yao (2008), Regional seismic characteristics of the 9 October 2006 North Korean nuclear test, *Bull. Seismol. Soc. Am.*, *98*(6), 2571–2589, doi:10.1785/0120080128.

Zhao, L. F., X. B. Xie, W. M. Wang, J. H. Zhang, and Z. X. Yao (2010), Seismic *Lg*-wave *Q* tomography in and around Northeast China, *J. Geophys. Res.*, *115*, B08307, doi:10.1029/2009JB007157.

Zhao, L. F., X. B. Xie, W. M. Wang, and Z. X. Yao (2012), Yield estimation of the 25 May 2009 North Korean nuclear explosion, *Bull. Seismol. Soc. Am.*, *102*(2), 467–478, doi:10.1785/0120110163.

Zhao, L. F., X. B. Xie, J. K. He, X. B. Tian, and Z. X. Yao (2013a), Crustal flow pattern beneath the Tibetan plateau constrained by regional Lg-wave Q tomography, *Earth Planet. Sci. Lett.*, *383*, 113–122, doi:10.1016/j.epsl.2013.09.038.

Zhao, L. F., X. B. Xie, W. M. Wang, J. H. Zhang, and Z. X. Yao (2013b), Crustal Lg attenuation within the North China Craton and its surrounding regions, *Geophys. J. Int.*, *195*(1), 513–531, doi:10.1093/gji/ggt235.

Zhao, L. F., X. B. Xie, W. M. Wang, and Z. X. Yao (2014), The 12 February 2013 North Korean underground nuclear test, *Seismol. Res. Lett.*, *85*(1), 130–134, doi:10.1785/0220130103.

Zhao, L. S., M. K. Sen, P. Stoffa, and C. Frohlich (1996), Application of very fast simulated annealing to the determination of the crustal structure beneath Tibet, *Geophys. J. Int.*, *125*(2), 355–370, doi:10.1111/j.1365-246X.1996.tb00004.x.

Zheng, X. F., Z. X. Yao, J. H. Liang, and J. Zheng (2010), The role played and opportunities provided by IGP DMC of China National Seismic Network in Wenchuan earthquake disaster relief and researches, *Bull. Seismol. Soc. Am.*, *100*(5B), 2866–2872, doi:10.1785/0120090257.

Zhu, T. F., K. Y. Chun, and G. F. West (1991), Geometrical spreading and Q of Pn waves: An investigative study in eastern Canada, *Bull. Seismol. Soc. Am.*, *81*(3), 882–896.